12-1-2021

A Pipeline for Enhanced Multimodal 2D Imaging of Concrete Structures

Sina Mehdinia
Portland State University

Thomas Schumacher
Portland State University, thomas.schumacher@pdx.edu

Xubo Song
Oregon Health & Science University

Eric A. Wan
Portland State University, eric.wan@pdx.edu

Citation Details

Published as: Mehdinia, S., Schumacher, T., Song, X., & Wan, E. (2021). A pipeline for enhanced multimodal 2D imaging of concrete structures. *Materials and Structures*, *54*(6), 228. https://doi.org/10.1617/s11527-021-01803-w

A PIPELINE FOR ENHANCED MULTIMODAL 2D IMAGING OF CONCRETE STRUCTURES

Sina Mehdinia[1], Thomas Schumacher[1,*], Xubo Song[2], and Eric Wan[3]

[1] Department of Civil and Environmental Engineering, Portland State University, Portland, OR

[2] School of Medicine, Oregon Health and Science University, Portland, OR

[3] Department of Electrical Engineering, Portland State University, Portland, OR

* Corresponding author, E-mail: thomas.schumacher@pdx.edu

Abstract: We present an imaging pipeline to achieve enhanced images of the interior of concrete from ground penetrating radar (GPR) and ultrasonic echo array (UEA) measurements. This work lays the foundation for an advanced yet practical imaging tool to assess concrete structures. Specifically, we propose an enhanced two-dimensional (2D) total focusing method (XTFM) to reconstruct images from raw GPR and UEA data. The proposed XTFM algorithm integrates total focusing method (TFM) and synthetic aperture focusing technique (SAFT) concepts to post-process large independent and interelement measurements from both modalities in a computationally efficient way. Furthermore, we introduce a novel 2D image fusion algorithm using wavelet multilevel decomposition and an NDT knowledge-based rule to fuse GPR and UEA images. We then compare our algorithm with conventional fusion algorithms such as averaging, maximum, and product. The results from three laboratory concrete reference specimens are evaluated in detail. The fused images are compared with each other as well as benchmarked with

the original GPR and UEA images. The output image obtained from our proposed pipeline is an enhanced 2D image of the interior of concrete structures that eases interpretation by a human inspector as well as has it the potential to improve interpretation by computer vision and image analysis algorithms.

Keywords: Non-destructive testing, condition assessment, ground penetrating radar, ultrasonic echo array, image fusion, synthetic aperture focusing technique, total focusing method, pipeline, image evaluation metric, concrete structure.

INTRODUCTION AND BACKGROUND

It has been decades since imaging technologies first found their way into non-destructive testing (NDT) of concrete structures. Many NDT methods have been introduced to image the interior of concrete such as radar imaging [1, 2, 3], ultrasonic echo imaging [4, 5, 6], ultrasonic tomography [7, 8], X-ray computed tomography (CT) [9, 10], and magnetic resonance imaging (MRI) [11]. All these modalities have their own limitations [12, 13]. The two most used modalities for NDT of concrete structures are electromagnetic (or radar) waves and ultrasonic stress waves. Both have their strengths and weaknesses, stemming from their underlying physics principles [14]. For example, virtually all the energy of an electromagnetic wave produced by a ground penetrating radar (GPR) instrument is reflected when arriving at a metallic object such as a steel reinforcing bar (or rebar) in reinforced concrete. On the other hand, a significant portion is transmitted through concrete-air interfaces such as an internal crack or void. Conversely, ultrasonic stress waves can penetrate through a metallic object, but most of the energy is reflected at a concrete-air interface. Furthermore, scattering and attenuation patterns are different for these two modalities, so is the speed of data collection [15]. Langenberg et al. discuss the underlying theory of electromagnetic and ultrasonic stress wave imaging in the context of NDT on concrete [16].

Image fusion is the process of combining and merging complementary information into a single image from two or more source images, which generates an improved visualization, and benefits from different NDT methods, especially when they are complementary in nature [15]. There are two main reasons to perform multimodal image fusion [17]. The first one is to achieve an improved visual representation of an image with higher overall quality, thus improving a human inspector's ability to determine features of interest. The second one is to produce a single image that has the information content from both modalities for subsequent computer vision and image processing algorithms such as image segmentation. For multimodal image fusion, it is desirable to preserve relevant and complementary information while reducing noise and providing an enhanced visual representation [18]. In this study, image fusion is performed at the pixel level, where the fused image is obtained from the corresponding pixel values of the source images.

Kohl et al. [15] published the first research on data fusion of ultrasonic and GPR images on concrete where they evaluated different arithmetic rules such as mean, substitution, and maximum to fuse the images. In addition, they employed the maximum amplitude of both modalities on datasets of different sizes. The authors reported that maximum information content was achieved using their approach for concrete structures with high reinforcement density and/or air voids. They did not propose any metrics that would allow for evaluating image quality. In a similar study, Maierhofer et al. [19] performed data fusion of GPR and UEA data from concrete structures. The authors used the maximum amplitude method and reported that maximum information was obtained in structures with a high reinforcement density, tendon ducts, and/or air voids and gaps. Like [15], they did not use any metrics to quantify information or image quality. Van der Wielen et al. [20] used ultrasonic and GPR measurements on concrete pavement and compared the results. They found that GPR is more efficient for dowel positioning and found both useful in thickness estimation. Krause et al. [21] compared ultrasonic echo, GPR and impulse-echo methods on concrete. They compared the modalities in terms of measuring thickness, location of a metal duct and voided regions inside the duct. They found that all the modalities are useful in measuring thickness and location of the duct. They also found that GPR is not suitable to detect the voids inside the ducts while UEA is. Gucunski [22] et al. reported a comparison of some NDT methods including GPR and ultrasonic pulse echo in condition assessment of concrete bridge decks. They categorized different NDT technologies and reported that both GPR and ultrasonic pulse echo have good potential in detecting delaminations and deterioration. Wimsatt et al. [23] reported combining three datasets from ultrasonic echo, impact echo, and GPR obtained from tunnel inspection using weighted averaging. They applied depth-varying weights to each image to account for different resolutions and penetration depths. They reported that the fused images provide useful information from each modality in a concise combined presentation.

Salazar et al. used fusion of GPR and ultrasound images on a historic masonry wall using the mean and product results of the two images [24]. They reported improved defect detection in the fused image, especially with the mean method, but without the support of any image quality metrics. Not applied to images but related, Volker and Shokouhi applied two data fusion algorithms, namely Dempster's rule of combination and the Hadamard product for GPR, impact echo, and ultrasonic pulse echo data to automatically detect honeycombing in concrete [25]. They evaluated their method quantitatively by comparing receiver operating characteristic (ROC) curves for individual tests and fusion methods. Results from both fusion algorithms were slightly better compared to when a single modality was used. They also investigated clustering methods for fusing GPR, impact echo, and ultrasonic data to detect honeycombing in another study [26] and found that the density-based clustering algorithm performed well on the classification task between defect and non-defect features.

Summarizing the state-of-the-art in imaging of concrete structures, we make the following observations: (1) Reconstruction algorithms are not cohesive among GPR and UEA modalities, and hence there is a lack of well-defined holistic pipeline, (2) image fusion for concrete applications has still many opportunities for improvement, (3) few studies have proposed quantitative metrics to evaluate fusion performance, and (4) no advanced automated diagnostic algorithms have been developed to quantitatively analyze images.

The main contribution of this study is a comprehensive pipeline for enhanced multimodal 2D imaging of concrete structures that span the first three points above. First, we present an integrated algorithm to reconstruct GPR and UEA images from raw independent and interelement measurements. Second, we introduce a fusion algorithm based on multilevel wavelet decomposition and an NDT-informed fusion rule. Third, we evaluate the quality of each image in terms of two standard types of reflectors and compare the image quality between the original GPR, UEA and fused images. The overall goal is to lay the foundation for an advanced yet practical diagnostic imaging tool for concrete structures. This pipeline has the potential to be used in conjunction with image analysis methods such as deep learning to build a prognostics tool in the future if a proper amount of valid data is available.

EXPERIMENTAL SETUP

Test Specimens

Three specimens with different geometries and known features were built in the laboratory using a standard normal-weight concrete with a specified compressive strength of 31 MPa (4500 psi). The outside dimensions of all specimens are length x width x depth = 1219 x 610 x 305 mm (48 x 24 x 12 in). **Fig. 1** (a) shows Specimen 1, which is unreinforced and varies in depth from 51 to 305 mm (2 to 12 in) in steps of 51 mm (2 in). **Fig. 1** (b) shows Specimen 2, which contains five #4 [bar diameter, d_b = 13 mm (0.5 in)] steel rebars having rebar clear covers, c_c on the top and bottom side ranging from 25 to 127 mm (1 to 5 in) and 165 to 267 mm (6.5 to 10.5 in), respectively. Finally, Specimen 3, which is shown in **Fig. 1** (c), has a row of rebars on each the top and bottom side with a constant rebar clear cover, c_c = 76 mm (3 in). The rebars on the top and bottom side range from #4 to #8 [d_b = 12.7 to 25 mm (0.5 to 1 in)] and #9 to #11 [d_b = 29 to 36 mm (1.13 to 1.41 in)]. The bottom side also has four closely-spaced #4 [d_b = 13 mm (0.5 in)] rebars as well as a hollow 51 mm (2 in) diameter PE pipe.

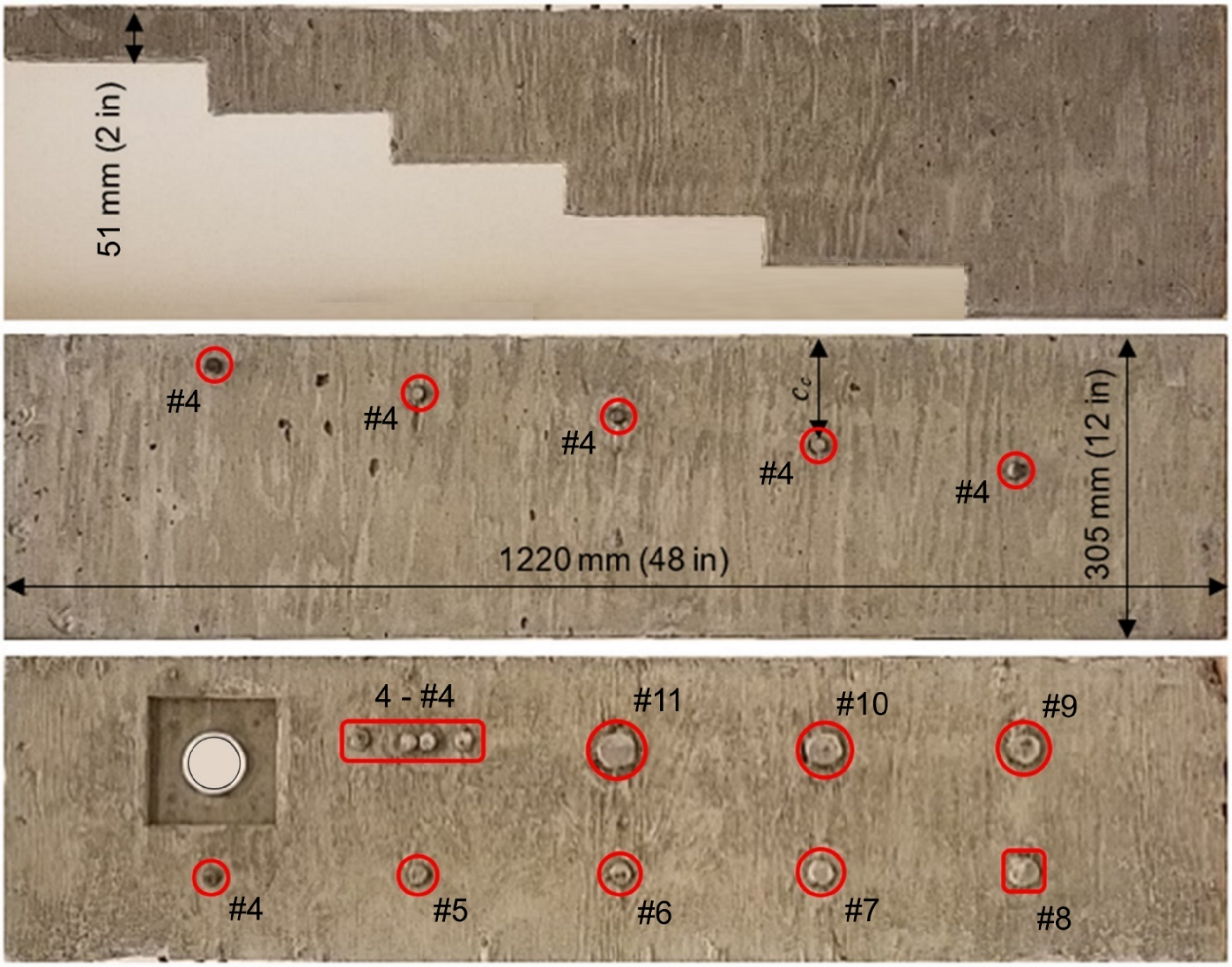

Fig. 1 – Photos (rectified elevations views) of three reference specimens (top to bottom): Specimens 1, 2, and 3. Rebars are highlighted with red circles/rectangles.

METHODOLOGY

Instruments and Data Collection

Two measurement modalities are utilized in this research both using a pitch-catch configuration: electromagnetic waves and ultrasonic stress waves. For the electromagnetic waves, a hand-held ground penetrating radar (GPR) instrument from GSSI, Model StructureScan Mini XT was employed [see photo in **Fig. 2** (a)]. The instrument is equipped with one transmitting and one receiving antenna (subsequently referred to as transducer). It emits an electromagnetic pulse that is transmitted into the material along a path on the structure's surface, as shown on the photo in **Fig. 2** (c). A portion of the incident electromagnetic pulse is reflected at interfaces between materials with different dielectric properties [14]. **Fig. 2** (b) and (d) show a typical individual measurement (or A-scan signal) and a contour plot of subsequent A-scan signals (or B-scan plot), respectively, of unprocessed GPR data. Technical details are provided in **Table 1**.

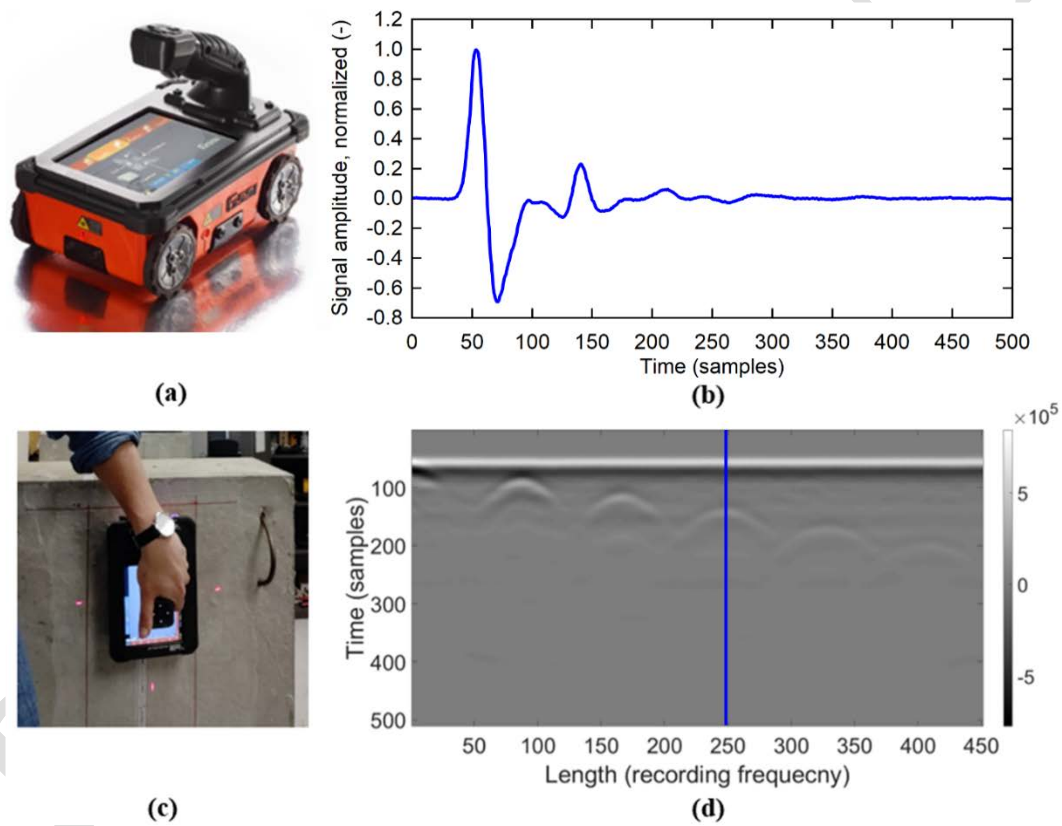

Fig. 2 – Ground penetrating radar (GPR) measurements: (a) Photo of instrument (Manufacturer, model: GSSI, StructureScan Mini XT), (b) typical A-scan signal (unprocessed), (c) Photo taken during data collection, and (d) typical B-scan plot from independent measurements (unprocessed). The blue line in (d) marks the location of the A-scan signal shown in (b).

For the ultrasonic stress waves, an ultrasonic echo array (UEA) instrument from Proceq, Model Pundit 250 Array, was used [see photos in **Fig. 3** (a) and (c)]. The instrument is equipped with 24 ultrasonic transducers, arranged in an 8 x 3 array. It emits a shear stress wave pulse row-by-row into the material, which is subsequently received by all other transducers. A portion of the incident stress wave is reflected at interfaces between materials with different acoustic impedances [14]. **Fig. 3** (b) and (d) show a typical A-scan signal and B-scan plot, respectively of unprocessed ultrasonic echo data. The transducer frequency is 50 kHz with a sampling frequency of 1 μs. **Table 1** shows a comparison between the properties of the GPR and UEA instruments.

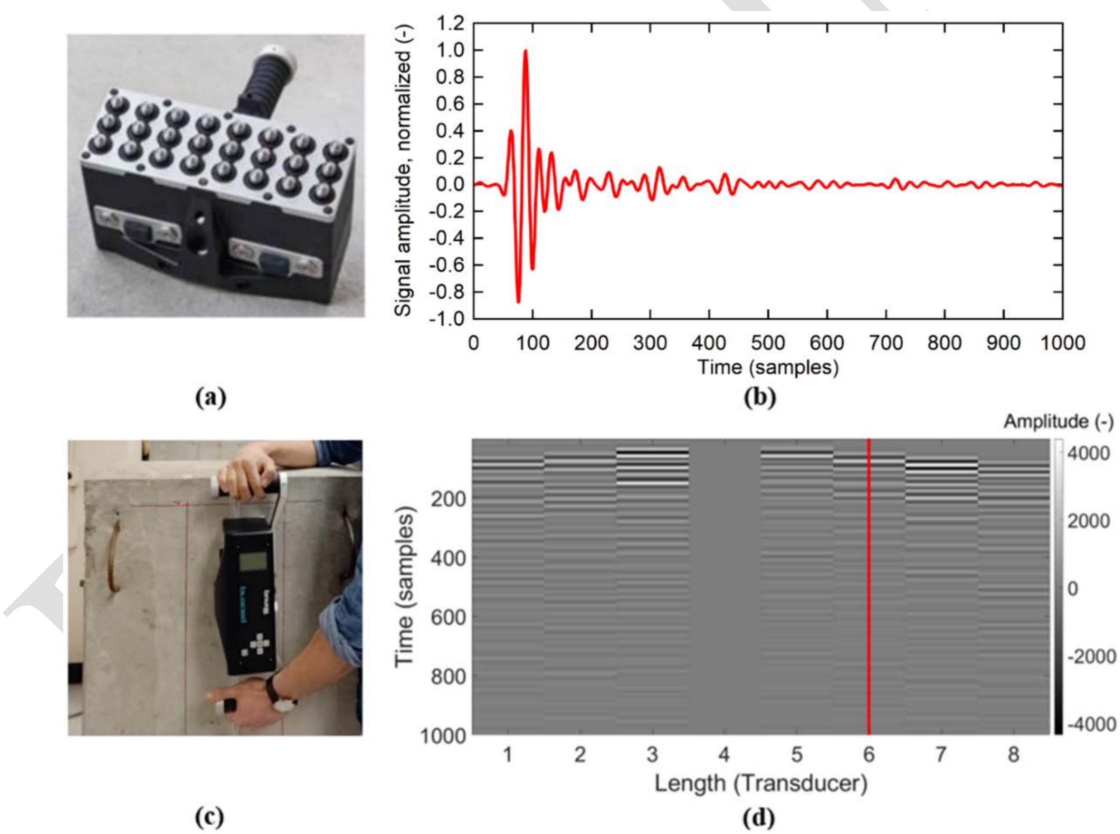

Fig. 3 – Ultrasonic echo array (UEA) measurements: (a) Photo of instrument (Manufacturer, model: Proceq, Pundit 250 Array); (b) typical A-scan signal (unprocessed), (c) Photo taken

during data collection, and (d) typical B-scan plot from interelement measurements (unprocessed). The red line in (d) marks the location of the A-scan signal shown in (b).

Table 1 – Technical details of the two utilized instruments.

Instrument	GPR	UEA
Wave type	Electromagnetic	Stress (shear) wave
Central pulse frequency	2.7 GHz	50 kHz
Signal Resolution	0.0164 ns	1 μs
Recording frequency	2.54 mm (0.1 in) (fixed)	10 mm (0.394 in) (selected for this study)
Number of transducer rows, transducers/row	2, 1	8, 3[1]
Transducer spacing(s)	40 mm (1.58 in)	30 mm (1.18 in)

[1]The instrument records across all three transducers in one row and then computes and saves the average signal.

PIPELINE METHODOLOGY

Image Reconstruction

In this research, an integrated approach based on the total focusing method (TFM) [27, 28] and the synthetic aperture focusing technique (SAFT) [4] was employed that can be used to reconstruct 2D images for both modalities. TFM utilizes the full aperture to reconstruct the image by synthetically focusing on every pixel of interest, while SAFT uses independent recordings [29, 30]. Our reconstruction approach uses measurements that contain both interelement data of the array as well as independent overlapping measurements and works for both GPR and UEA modalities. We propose the term XTFM (extended total focusing method) because it considers overlapping measurements and works across modalities, i.e., it can process both GPR and UEA data. Overlapping measurements return an independent array response at different positions where there is a dependent interelement response at each position. Therefore, a large matrix of measurements is collected that contains both interelement as well as independent array data. We treat each UEA measurement the same as one GPR recording where the UEA data are stored in the form of an nS x 1000 x 8×8 array, while The GPR data are in a nS x 512 x 2×2 array, with the diagonals consisting of zeros and the matrix being symmetric, meaning that only one signal is recorded between each transducer pair. nS is the total number of scans. For every measurement, the image area that can be covered by the signal length is used for reconstruction. Thus, the beam is not focused in any particular manner. We deliberately omit the enveloping of the signal (using the Hilbert Transform) that is often applied in practice since we find that it creates the illusion of a circular shape for circular objects like rebars. It should be noted that the GPR instrument used in this study is not an array GPR (it has only one emitter and receiver), however, our proposed XTFM algorithm works for any number of channels ≥ 2. The following pseudo-code shows the steps of the proposed algorithm. The actual code in Python and MATLAB can be downloaded at no cost from our GitHub repository [31].

Algorithm 1: Pseudocode for 2D XTFM

XTFM (**X**, *v*, *ε*, *sR*, *d*, s, *r, dim*)

Input:

X: 4D matrix of raw measurements containing all slices of independent and interelement data with the format of *nS* sL * nC * nC* , where *nS* is the number of independent scans, *sL is the signal length of a raw measurement* and *nC* is the number of channels of the instrument.

v: velocity of the medium

ε: time offset

sR: signal resolution

d: recording frequency

s: transducer spacing

r: desired resolution

dim: grid dimensions (2D)

Output: I (reconstructed image)

Initialize vectors, $\mathbf{x_n}$, $\mathbf{y_n}$ spanning from 0 to *dim* *r with a step of *r*

Initialize the output image, **I** with zeros with a size of *dim*

For every *k* independent measurement (total of *nS*)

For every *i, j* interelement measurement (total of (*nC* * *(nC-1)/2*):

Calculate T matrix = $$\left[\left(\frac{\sqrt{(x_n\text{-}i*s - k*d)^\wedge 2+y_n{}^\wedge 2))+}\sqrt{(x_n\text{-}j*s - k*d)^\wedge 2+y_n{}^\wedge 2}}{v}+\varepsilon\right)/sR\right]$$

Mask T matrix to discard out of range values (values bigger than *sL*)

Add X[*k*,**T***, i, j*] to **I**

End For

End For

Return I

The time variable, $\mathbf{T}$, is an array, computed by broadcasting the $\mathbf{x}_n$ and $\mathbf{y}_n$ vectors. The array $\mathbf{T}$ can be implemented using fancy indexing (i.e., passing an array of indices to access elements of an array at the same time) and broadcasted to the final image. Thus, it can make the process computationally more efficient. All indices in the $\mathbf{T}$ matrix contribute to the final image if they are less than the signal length. The other indices are discarded through the masking step. This can lead to adding more information to the image, as well as increasing the risk of adding potential artifacts. Both ε and v need to be determined experimentally, which aligns the images in the y-direction and results in the correct focus. The process involves tuning the two parameters until the known features such as rebars and the backwall are shown in their correct locations. The assumption is that both parameters are deterministic entities and can be applied uniformly throughout a specimen. While this is a reasonable assumption for the specimens used in our study, it might not be for a real structure with larger dimensions where concrete properties might vary spatially.

Image Fusion

Preprocessing

To keep the pipeline practical and general, an effort was made to minimize any manual preprocessing. The images should be aligned (or registered) correctly in the y-direction when the parameters ε and v were tuned correctly. Based on the geometry of the instruments and measurements, there might be a slight misalignment in the x-direction. Thus, the only image registration necessary in the x-direction before fusing the GPR and UEA images is translation in the x-direction. Finally, a conventional (and optional) surface wave removal was applied to both GPR and UEA images and the images were min-max normalized to take amplitude values in the 0 to 1 range.

Wavelet image fusion

Wavelet image fusion is a multiresolution approach capable of handling different image resolutions while extracting the image content with the most pertinent information [32, 33, 34]. The fusion rule used here was informed by the nature of the measurements. The direct pulse recorded from a reflector follows one of these two patterns, which consist of a center and two side lobes: dark-bright-dark (i.e., low-high-low intensity), which we name Type 1 reflector and a bright-dark-bright (i.e., high-low-high intensity), which we name Type 2 reflector. Examples of the former and latter are embedded metals such as rebars and air voids or backwalls of the concrete, respectively. The other areas of an image where there is no reflector are usually shades of gray having some level of variation, or noise. **Fig. 4** shows (a) a sample reconstructed image having both reflectors as well as (b) a representative A-scan with the two reflectors highlighted by boxes. Our objective is to achieve high contrast for both types of reflectors, Type 1 as well as Type 2, so that they are clearly discernible from the background. For example, in the results section we discuss that from reconstructed images of Specimen 2, the GPR image shows all the rebars but it does not reveal the backwall. On the other hand, the UEA image clearly shows the backwall but the small rebars are missing. Generally, we observe higher attenuation of the radar waves, stronger reflection of radar wave energy on near-surface rebars, and higher penetration depth of the ultrasonic waves.

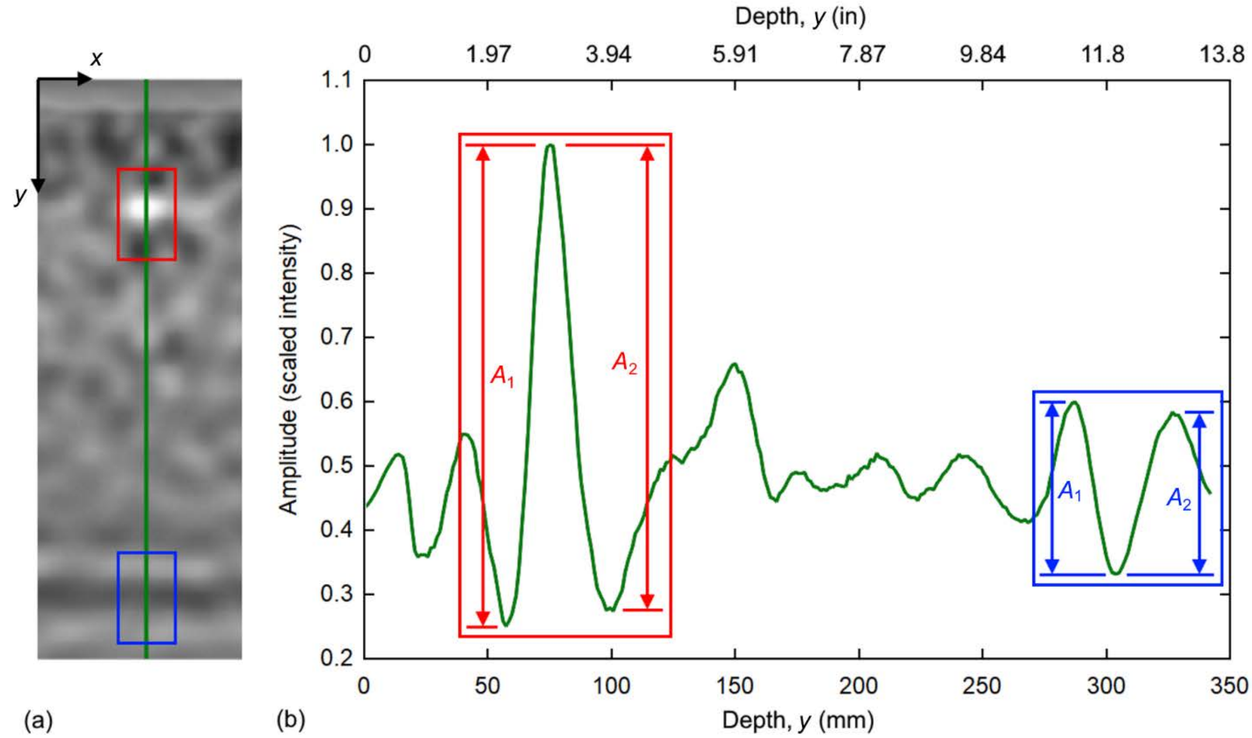

Fig. 4 – (a) Sample reconstructed image of Specimen 2 showing Type 1 (red box) and Type 2 (blue box) reflectors and (b) representative A-scan with the two reflectors highlighted by boxes [location indicated by green line in (a)].

We propose **Algorithm 2** based on the observations made from reconstructed 2D images of the three specimens and the underlying physics of the used modalities.

Algorithm 2: Proposed Image Fusion Algorithm

Step 1: Each image from the two modalities is decomposed via 2D multilevel wavelet decomposition into a low-frequency and three high-frequency detail coefficients for each level. The decomposition is performed recursively for a desired number of levels, for which we propose it being at least four. The Sym5 wavelet from the Symlets family is used in this study, which is suitable for 2D image processing applications [35].

Step 2: Each approximation is divided into three ranges of bright, dark, and gray based on the intensity of each pixel value. The thresholds to divide these three ranges are: pixel values > mean + one standard deviation, pixel values < mean - one standard deviation, and pixel values within mean +/- one standard deviation, respectively. The following rules are applied, based on the expected capabilities and reliabilities of the two modalities:

Case 1: If a feature is bright in the images of both modalities, e.g., the center lobe of a Type 1 reflector (e.g., a rebar in concrete), or the side lobes of a Type 2 reflector, we pick the maximum pixel value.

Case 2: If a feature is dark in the images of both modalities, e.g., the center lobe of a Type 2 reflector (e.g., the hollow pipe embedded in Specimen 3 or the backwall), or the side lobes of a Type 1 reflector, we select the minimum pixel value.

Case 3: If a bright feature is visible in the GPR image, and in the UEA image it is in the gray (i.e., mid-) range, we pick the pixel value from the GPR image.

Case 4: If a bright feature is visible in the UEA image and the GPR image shows it in the gray range, we select the mean value, since GPR is better suited for detecting bright reflectors (like a rebar).

Case 5: If a dark feature is visible in the GPR image and the UEA image shows it in the gray range, we pick the mean value.

Case 6: If a dark reflector is visible in the UEA image and the GPR image shows it in the gray range (like the backwall in Specimens 2 and 3), we select the pixel value from the UEA image.

Case 7: If a feature appears in the gray range in the images of both modalities, we pick the mean pixel value.

Case 8: If a feature is in the bright range of the GPR image and the dark range of UEA image, we select the pixel value of the bright feature.

Case 9: If a feature is in the bright range of the UEA image and dark range of the GPR image, we select the mean pixel value.

Step 3:

Adopt the maximum pixel value of the detail coefficients.

Step 4:

Perform multilevel wavelet reconstruction using the inverse wavelet transform to obtain the final fused image.

RESULTS AND DISCUSSION

Local Evaluation Metric

The aim of fusion is to enhance the quality (discernibility) of the features of interest and provide a single overall high-quality image capturing information from both modalities. Therefore, we suggest two types of metrics to evaluate the fused images. First, and the more important one, is a local metric to evaluate each reflector individually. As previously described, there are two types of reflectors with consecutive bright and dark regions. To measure the quality of a feature, we define a local contrast metric for each reflector as the contrast (relative intensity) of the local extrema on top of the feature. We measure this by adding relative intensities of the extrema amplitudes. **Fig. 4** (b) shows the amplitudes that are added together (e.g., $|A_1|+|A_2|$) to compute the value of the local contrast metric. This metric measures the saliency of the center lobe of the recorded pulse. Red and blue lines refer to Type 1 and Type 2 reflectors, respectively.

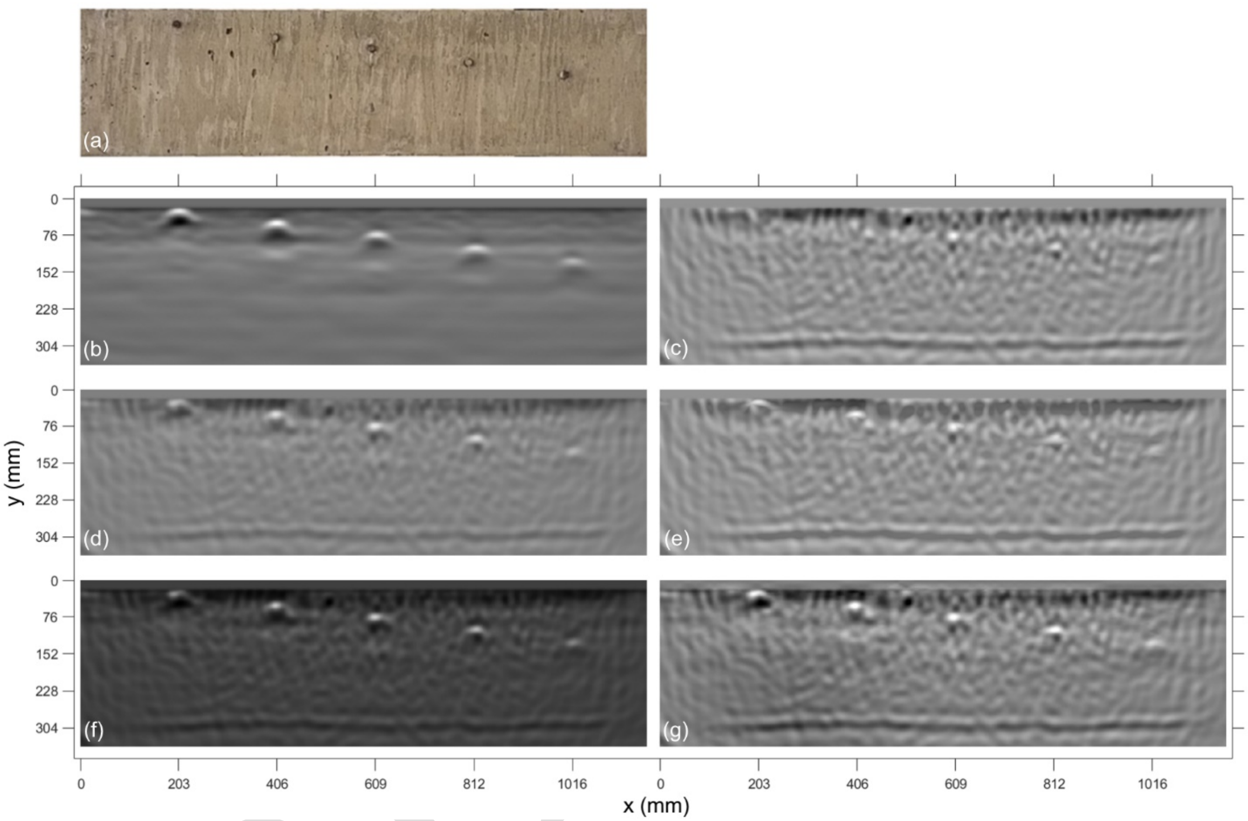

Fig. 5 – Results for Specimen 2: (a) Photo, reconstructed images from (b) GPR and (c) UEA, and fused images using (d) averaging, (e) maximum, (f) product, and (g) our proposed method.

Table 2 – Normalized local evaluation metrics for select image features from Specimen 2.

Case	Position: *x*, *y* in (mm)	GPR	UEA	Average	Maximum	Product	Proposed method
#4 rebar	8, 1 (203, 25)	**1.00**	0.00	0.45	0.56	0.46	**1.01**
#4 rebar	16, 2 (406, 51)	**1.00**	0.52	0.75	0.79	0.87	**1.08**
#4 rebar	24, 3 (610, 76)	0.86	**1.00**	0.90	0.98	**1.12**	**1.23**
#4 rebar	32, 4 (813, 102)	**1.00**	0.83	0.85	0.82	**1.05**	**1.29**
#4 rebar	40, 5 (1016, 127)	**1.00**	0.83	0.83	0.82	**0.98**	**1.23**
Backwall	28.8, 12 (730, 305)	0.00	**1.00**	0.49	0.89	0.42	**1.05**

From **Table 2** and **Fig. 5** we can observe that the GPR image [**Fig. 5** (b)] clearly shows small rebars at different depths, while the UEA image [**Fig. 5** (c)] does not reveal small and close-to-the-surface rebars. The results in the **Table 2** are normalized with respect to the best individual modality to show if any of the fusion methods can retain or improve the evaluation metric. Average and maximum [**Figs. 5** (d) and (e)] do not perform better than any of the single modalities while product [**Fig. 5** (f)] sometimes gives better results, especially when both modalities detect the rebar. However, product fails when one modality does not detect it and when information is complementary. In the case of a backwall, the information is complementary and averaging and product perform worse than maximum. Our proposed method [**Fig. 5** (g)] can preserve and accentuate information in all the above cases.

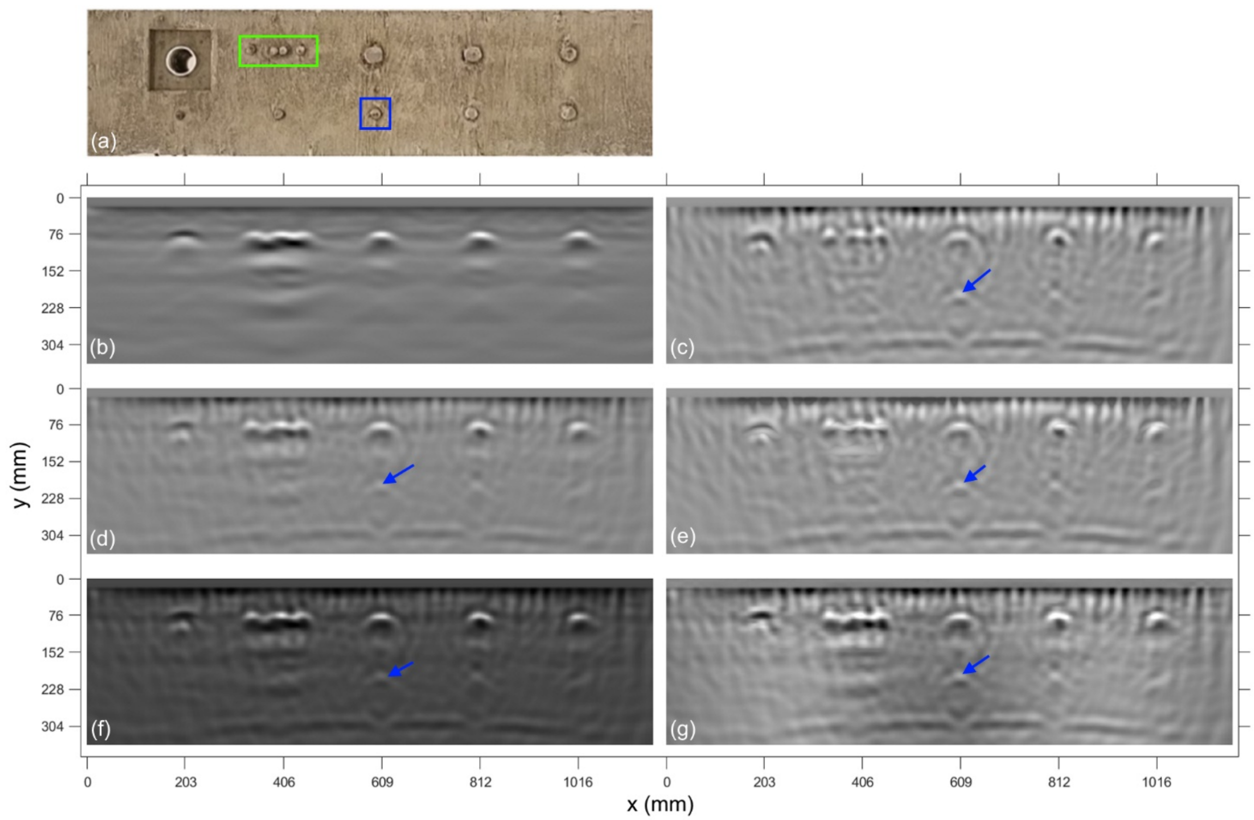

Fig. 6 – Results for Specimen 3: (a) Photo, reconstructed images from (b) GPR and (c) UEA, and fused images using (d) averaging, (e) maximum, (f) product, and (g) our proposed method.

Table 3 – Normalized local evaluation metric for reconstructed images for Specimen 3.

Case	Position: *x*, *y* in (mm)	GPR	UEA	Average	Maximum	Product	Proposed method
#11 rebar	24, 3 (610, 76)	**1.00**	0.63	0.81	0.79	**1.08**	**1.03**
#10 rebar	32, 3 (813, 76)	**1.00**	0.76	0.80	0.89	**1.01**	**1.12**
# 9 rebar	40, 3 (1016, 76)	**1.00**	0.84	0.84	0.84	**1.09**	**1.36**
# 6 rebar	24, 8.5 (610, 216)	0.00	**1.00**	0.57	0.93	0.60	**1.09**
Backwall	28.8, 12 (730, 305)	0.12	**1.00**	0.54	0.87	0.52	**0.99**
Pipe	8, 3 (203, 76)	0.89	**1.00**	0.75	0.91	0.76	**1.46**
Close rebars	13.75-17.75, 3 (349-451, 76)	0.62	**1.00**	0.67	0.63	**1.14**	**1.19**

From **Fig. 6** And **Table 3** we can see that both GPR and UEA images [**Figs. 6** (b) and (c)] clearly show the large diameter rebars that are located close to the surface. In this case, averaging, maximum, and product [**Figs. 6** (d) to (f)] are all able to detect the features as well, while product giving a better result, since the feature is detected in both modalities and multiplying them accentuates redundant information. The proposed method [**Figs. 6** (g)] can retain the information from both modalities and gives the best results. In case of the #6 rebar at a depth of 216 mm (8.5 in) that is hidden under the #11 top rebar [see blue box in **Fig. 6** (a)], as expected, the GPR image [**Fig. 6** (b)] does not show the rebar since all the energy is reflected back from the top rebar. However, the UEA image [**Fig. 6** (c)] reveals this feature (see blue arrow) because stress waves can propagate through metallic objects. In this case, averaging, maximum, and product [**Fig. 6** (d) to (f)] give worse results compared to when only a single modality, e.g., UEA, is used, hence no value is added with fusion. However, the proposed method [**Fig. 6** (g)] not only retains the information but also has a slightly improved contrast value. In the case of Type 2 reflectors, i.e., the pipe and the backwall, we can see that the GPR image [**Fig. 6** (b)] barely shows the backwall. Again, none of the fusion methods give better results than the best individual modalities, which is UEA in this case, but the proposed method [**Fig. 6** (g)] retains the information of the backwall and intensifies the pipe. The fusion rule is to keep the minimum value when both modalities detect a dark feature or trust UEA when the UEA image shows a dark feature while the GPR image shows it in gray. For closely spaced rebars [see green box in **Fig. 6** (a)], we also study a horizontal line at y = 76 mm (3 in) and consider the relative contrast of the rebars as well as the relative contrast of the space between the rebars. We can see that the UEA image [**Fig. 6** (b)] is better than the GPR image [**Fig. 6** (c)], and among the fusion methods, product [**Fig. 6** (f)] and our proposed method [**Fig. 6** (g)] exhibit the best performance. It should be noted that none of the images allow for distinguishing the two middle bars, which are in contact with each other, i.e., all images show three rather than four individual reflectors. This is a limitation of our instruments and their resulting wavelength in our concrete.

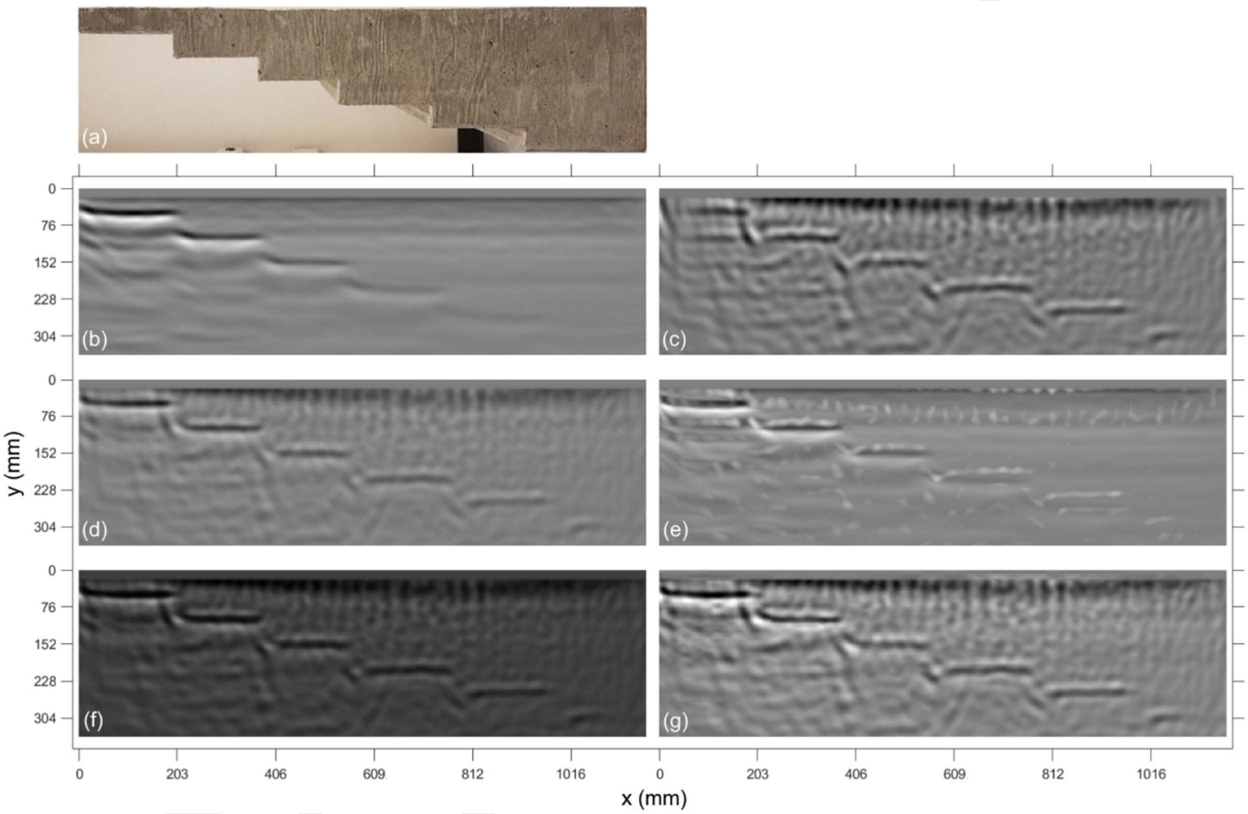

Fig. 7 – Results for Specimen 1: (a) Photo, reconstructed images for (b) GPR and (c) UEA, and fused images using (d) Averaging, (e) Maximum, (f) Product, and (g) our proposed method.

Table 4 – Normalized local evaluation metric for images from Specimen 1.

Case	Position: *x*, *y* in (mm)	GPR	UEA	Average	Maximum	Product	Proposed method
Step 1	4, 2 (102, 51)	**1.00**	0.46	0.68	0.74	0.55	**1.08**
Step 2	11.5, 4 (292, 102)	0.84	**1.00**	0.88	**1.06**	0.82	**1.06**
Step 3	18.5, 6 (470, 152)	0.57	**1.00**	0.75	0.61	0.73	**0.97**
Step 4	26, 8 (660, 203)	0.38	**1.00**	0.66	0.57	0.65	**0.99**
Step 5	34, 10 (864, 254)	0.19	**1.00**	0.47	0.38	0.49	**1.01**
Step 6	43, 12 (1092, 305)	0.32	**1.00**	0.55	0.82	0.57	**0.98**

From **Table 4** and **Fig. 7** we can see that the UEA image [**Fig. 7** (c)] shows the backwalls (steps) consistently better than the GPR image [**Fig. 7** (b)] except for the one very close to the surface. The proposed method [**Fig. 7** (g)] can retain and improve the information in most of the cases better than any of the other methods [**Figs. 7** (d) to (f)].

Global Evaluation Metrics

While we have now evaluated image quality based on local metrics, it can be valuable to consider some global evaluation metrics. Although we humans usually pay attention to local features and salient points in the image, we care about the overall appearance of the image as well. In addition, we would like to determine the overall information content of an image as well. These global metrics of quality are important for future work on automating the pipeline since image analysis methods such as deep neural networks perform notably worse when input images have a low quality [36]. In this study we used standard deviation, entropy, and average gradient as global evaluation metrics.

The standard deviation of a gray-level image represents the overall contrast. Usually, higher contrast images are more favorable for human perception because the features are more clearly discernible from the background [37]. **Table 5** shows the results for the standard deviation metric of all reconstructed images for all three specimens. Values were computed for the entire images shown in **Figs. 5** to **7** and then normalized relative to the highest individual modality. The fused image with the proposed method has a higher contrast compared to all other images.

Image entropy is used to measure the information content and richness of a grayscale image [37, 38]. **Table 5** shows the results for the entropy metric. The values are normalized relative to the highest individual modality. The proposed wavelet-based method produces an image with the highest information entropy among all images, which supports a visual analysis of the image where we can observe more details of rebars and backwall information.

Average gradient is an image fusion metric where spatial resolution of an image can be compared to other images [32]. Each pixel of the gradient image shows how the intensity changes in a given direction. We expect a higher average gradient for an image with more edges and features. **Table 5** shows the results of the average gradient metric for the different images. The values are normalized relative to the highest individual modality. It can be observed that the proposed wavelet-fused image has a higher average gradient, which means they contain more discernible features. This is consistent with a visual analysis, especially for the case of the proposed wavelet-based image where we can perceive more discernible features.

We can see that the proposed method performs well for all three global metrics and for all specimens. While maximum was not the best method when evaluated locally, it gives high global information, which makes sense since it maximizes information. However, it is unable to perform well globally for Specimen 1 when we have only Type 2 reflectors. This is because maximizing is not desired when the extremes are local minima. Even though product gives a high result in some cases, it does not perform well globally. Averaging, as expected by its definition, averages the information. We can see that the proposed method is able to retain the information from both modalities and accentuates them.

Table 5 – Normalized global evaluation metrics for images of all specimens.

Specimen	Global Metric	GPR	UEA	Average	Maximum	Product	Proposed method
1	Standard Deviation	0.80	**1.00**	0.72	0.74	0.68	**1.21**
2	Standard Deviation	0.70	**1.00**	0.68	0.91	0.65	**1.16**
3	Standard Deviation	0.82	**1.00**	0.77	**0.95**	0.77	**1.34**
1	Entropy	0.91	**1.00**	0.91	0.91	0.91	**1.05**
2	Entropy	0.88	**1.00**	0.89	**0.99**	0.88	**1.05**
3	Entropy	0.92	**1.00**	0.91	**1.00**	0.92	**1.12**
1	Average Gradient	0.60	**1.00**	0.62	0.67	0.62	**1.17**
2	Average Gradient	0.50	**1.00**	0.57	**0.96**	0.54	**1.12**
3	Average Gradient	0.64	**1.00**	0.67	**0.97**	0.67	**1.18**

SUMMARY AND CONCLUSIONS

In this article, a pipeline to image the interior of concrete structures is proposed and evaluated. Three laboratory concrete specimens with known geometry, material properties, and features were employed to evaluate the entire methodology. Data were collected for two different modalities using two commonly used non-destructive testing (NDT) instruments, namely ground penetrating radar (GPR) and ultrasonic echo array (UEA). An extended total focusing method (XTFM) was developed to reconstruct 2D images for both measurement modalities. A novel fusion algorithm based on multilevel wavelet decomposition and an NDT-informed rule was developed to fuse the GPR and UEA images. Image quality metrics were utilized enabling a quantitative comparison of the fused images in terms of local feature contrast and overall global quality. The results show that advanced image fusion has significant potential to enhance concrete imaging compared to when only individual GPR or UEA images are used. We made the following observations:

1. For the close-to-surface Type 1 reflectors (e.g., rebars) as well as small Type 1 reflectors, GPR is the superior modality, while UEA gives decent results except for small rebars close to the surface.
2. For Type 2 reflectors (e.g., pipe, backwall) UEA performs better than GPR, while GPR gives decent results, especially if the reflector is not very far from the surface.
3. If a metallic reflector is blocked by another metallic reflector, GPR is not able to detect it while UEA can.
4. For closely spaced rebars, UEA is performing better than GPR in differentiating the intensity in the space between rebars as well as keeping a high relative amplitude for the reflector.
5. The averaging fusion method keeps the information from both modalities, while smoothing everything. The maximum method does not produce consistent results and usually fails to improve an image. The reason is that the signals have multiple oscillations and there is usually a mismatch in many portions of the signals. Also, in case of Type 2 reflectors, maximization is not desired. The product method sometimes gives promising results, in particular for the cases when both modalities detect a Type 1 reflector. However, it fails in

almost all other cases such as when the information is complementary (i.e., one modality detects a feature and the other one does not), and when the reflector is Type 2.

6. The proposed wavelet method takes advantage of low pass filtering the images first to smooth the images and minimize undesired non-feature extrema (oscillations) and then apply a custom fusion rule, that maximizes, minimizes and averages pixel values depending on the type of reflector. In addition, high pass filtering images and maximizing details improves amplitude and relative contrast. This method has shown promise in all the cases covered in this study.

In conclusion, the proposed pipeline produced enhanced 2D images that retain and accentuate the information from both modalities with a target of Type 1 and Type 2 reflectors for all three specimens. We see significant potential and opportunity for further research, taking full advantage of the latest advances in the fields of image fusion and machine learning. The next step will be to collect additional data from specimens with known defects such as different types of cracking, rebar corrosion, and other forms of degradation. The fusion algorithm will also be tested and evaluated on large-scale laboratory specimens that exhibit different levels of damage from loading. Our ultimate goal is to develop a practical diagnostic tool that can be used to automatically analyze images and assist an inspector in the condition assessment of concrete structures.

SHARING OF DATA AND ALGORITHMS

All data and algorithms presented in this article will be available on the following GitHub repository [31]: https://github.com/Sinamhd9/A-Pipeline-for-Enhanced-Multimodal-Imaging-of-Structural-Concrete.

ACKNOWLEDGEMENTS

The technical support by GSSI for accessing raw data from the GPR instrument is appreciated. We further thank Ewen Carcreff from TPAC for his insights on ultrasonic phased array data processing and visualization. All measurements were carried out at the Infrastructure Testing and Applied Research Laboratory (*i*STAR) at Portland State University.

COMPLIANCE WITH ETHICAL STANDARDS

This research received partial support jointly by a 2018 seed grant from the Oregon Health and Science University and Portland State University. The authors declare that they have no conflict of interest.

REFERENCES

[1] Clem, D. J., Schumacher, T., & Deshon, J. P. (2015). A consistent approach for processing and interpretation of data from concrete bridge members collected with a hand-held GPR device. *Construction and Building Materials*, 86, 140-148.

[2] Sun, H., Pashoutani, S., & Zhu, J. (2018). Nondestructive evaluation of concrete bridge decks with automated acoustic scanning system and ground penetrating radar. *Sensors*, 18(6), 1955.

[3] Lai, W. W. L., Derobert, X., & Annan, P. (2018). A review of Ground Penetrating Radar application in civil engineering: A 30-year journey from Locating and Testing to Imaging and Diagnosis. *NDT & E International*, 96, 58-78.

[4] Schickert, M., Krause, M., & Müller, W. (2003). Ultrasonic imaging of concrete elements using reconstruction by synthetic aperture focusing technique. *Journal of Materials in Civil Engineering*, 15(3), 235-246.

[5] Krause, M., Mielentz, F., Milman, B., Müller, W., Schmitz, V., & Wiggenhauser, H. (2001). Ultrasonic imaging of concrete members using an array system. *NDT & E International*, 34(6), 403-408.

[6] Bittner, J. A., Spalvier, A., & Popovics, J. S. (2018). Internal Imaging of Concrete Elements. *Concrete International*, 40(4), 57-63.

[7] Choi, H., & Popovics, J. S. (2015). NDE application of ultrasonic tomography to a full-scale concrete structure. IEEE transactions on ultrasonics, ferroelectrics, and frequency control, 62(6), 1076-1085.

[8] Choi, H., Bittner, J., & Popovics, J. S. (2016). Comparison of ultrasonic imaging techniques for full-scale reinforced concrete. *Transportation Research Record*, 2592(1), 126-135.

[9] Balázs, G. L., Lublóy, É., & Földes, T. (2018). Evaluation of concrete elements with X-ray computed tomography. *Journal of Materials in Civil Engineering*, 30(9), 06018010.

[10] Moosavi, R., Grunwald, M., & Redmer, B. (2020). Crack detection in reinforced concrete. *NDT & E International*, 109, 102190.

[11] Marfisi, E., Burgoyne, C. J., Amin, M. H. G., & Hall, L. D. (2005). The use of MRI to observe the structure of concrete. *Magazine of concrete research*, 57(2), 101-109.

[12] Pla-Rucki, G.F. and Eberhard, M.O., (1995) “Imaging of reinforced concrete: State-of-the-art review.” *Journal of Infrastructure Systems*, Vol. 1(2), pp: 134-141.

[13] Büyüköztürk, O., (1998). “Imaging of concrete structures.” *NDT & E International*, Vol. 31(4), pp: 233-243.

[14] ACI-American Concrete Institute. (2013). 228: 2R-13 Report on nondestructive test methods for evaluation of concrete in structures.

[15] Kohl, C., Krause, M., Maierhofer, C. and Wöstmann, J., (2005). “2D-and 3D-visualisation of NDT-data using data fusion technique.” *Materials and Structures*, Vol. 38(9), pp: 817-826.

[16] Langenberg, K.J., Mayer, K. and Marklein, R., (2006). “Nondestructive testing of concrete with electromagnetic and elastic waves: Modeling and imaging.” *Cement and Concrete Composites,* Vol. 28(4), pp: 370-383.

[17] Li, H., Manjunath, B.S. and Mitra, S.K., (1995). “Multisensor image fusion using the wavelet transform.” *Graphical models and image processing*, Vol. 57(3), pp: 235-245.

[18] Nikolov, S., Hill, P., Bull, D. and Canagarajah, N., (2001). “Wavelets for image fusion.” *Wavelets in signal and image analysis* pp: 213-241. Springer, Dordrecht.

[19] Maierhofer, C., Zacher, G., Kohl, C., & Wöstmann, J. (2008). Evaluation of radar and complementary echo methods for NDT of concrete elements. *Journal of Nondestructive Evaluation*, 27(1-3), 47.

[20] Van der Wielen, A., Lybaert, M. and Grégoire, C., (2017). “Combined GPR and ultrasonic tomography measurements for the evaluation of a new concrete pavement.” *Proc. 9th International Workshop on Advanced Ground Penetrating Radar (IWAGPR),* IEEE, pp: 1-6.

[21] Krause, M., Bärmann, M., Frielinghaus, R., Kretzschmar, F., Kroggel, O., Langenberg, K.J., Maierhofer, C., Müller, W., Neisecke, J., Schickert, M. and Schmitz, V., (1997).

Comparison of pulse-echo methods for testing concrete. *NDT & E International*, Vol. 30(4), pp: 195-204.

[22] Gucunski, N., & National Research Council. (2013). *Nondestructive testing to identify concrete bridge deck deterioration*. Transportation Research Board.

[23] Wimsatt, A., White, J., Leung, C., Scullion, T., Hurlebaus, S., Zollinger, D., ... & Tonon, F. (2014). *Mapping voids, debonding, delaminations, moisture, and other defects behind or within tunnel linings* (No. SHRP 2 Report S2-R06G-RR-1).

[24] Salazar, A., Gosalbez, J., Safont, G. and Vergara, L., (2012). "Data fusion of ultrasound and GPR signals for analysis of historic walls". *IOP Conference Series: Materials Science and Engineering*, IOP Publishing, Vol. 42(1), p: 012008.

[25] Völker, C., & Shokouhi, P. (2015). Multi sensor data fusion approach for automatic honeycomb detection in concrete. *NDT & E International*, 71, 54-60.

[26] Völker, C., & Shokouhi, P. (2015). Clustering based multi sensor data fusion for honeycomb detection in concrete. *Journal of Nondestructive Evaluation*, 34(4), 32.

[27] Zhang, J., Drinkwater, B.W., Wilcox, P.D. and Hunter, A.J., (2010). "Defect detection using ultrasonic arrays: The multi-mode total focusing method." *NDT & e International*, Vol. 43(2), pp: 123-133.

[28] Holmes, C., Drinkwater, B.W. and Wilcox, P.D., (2005). "Post-processing of the full matrix of ultrasonic transmit–receive array data for non-destructive evaluation." *NDT & E International*, Vol. 38(8), pp: 701-711.

[29] Carcreff, E., Laroche, N., Braconnier, D., Duclos, A., & Bourguignon, S. (2017, September). Improvement of the total focusing method using an inverse problem approach. In *2017 IEEE international ultrasonics symposium (IUS)* (pp. 1-4). IEEE.

[30] Kerr, W., Rowe, P., & Pierce, S. G. (2017). Accurate 3D reconstruction of bony surfaces using ultrasonic synthetic aperture techniques for robotic knee arthroplasty. *Computerized Medical Imaging and Graphics*, 58, 23-32.

[31] Mehdinia, S. (2021). GitHub Repository: https://github.com/Sinamhd9/A-Pipeline-for-Enhanced-Multimodal-Imaging-of-Structural-Concrete.

[32] Daneshvar, S. and Ghassemian, H. (2010). “MRI and PET image fusion by combining IHS and retina-inspired models.” *Information Fusion*, Vol. 11(2), pp.114-123.

[33] Pajares, G., & De La Cruz, J. M. (2004). A wavelet-based image fusion tutorial. *Pattern recognition*, 37(9), 1855-1872.

[34] Balakrishnan, S., Cacciola, M., Udpa, L., Rao, B. P., Jayakumar, T., & Raj, B. (2012). Development of image fusion methodology using discrete wavelet transform for eddy current images. *NDT & E International*, 51, 51-57.

[35] Wang, A., Sun, H., & Guan, Y. (2006, April). The application of wavelet transform to multi-modality medical image fusion. In *2006 IEEE International Conference on Networking, Sensing and Control* (pp. 270-274). IEEE.

[36] Dodge, S., & Karam, L. (2017, July). A study and comparison of human and deep learning recognition performance under visual distortions. In 2017 26th international conference on computer communication and networks (ICCCN) (pp. 1-7). IEEE.

[37] Jagalingam, P., & Hegde, A. V. (2015). A review of quality metrics for fused image. *Aquatic Procedia*, 4(Icwrcoe), 133-142.

[38] Gonzalez, R.C. and Woods, R.E., (2008). “Digital image processing:” Pearson prentice hall. *Upper Saddle River, NJ*, 1.